REPORT

PEROVSKITE STRUCTURE

Stabilized tilted-octahedra halide perovskites inhibit local formation of performance-limiting phases

Tiarnan A. S. Doherty[1]†, Satyawan Nagane[1]†, Dominik J. Kubicki[1,2], Young-Kwang Jung[3], Duncan N. Johnstone[4], Affan N. Iqbal[1,5], Dengyang Guo[1,5], Kyle Frohna[1], Mohsen Danaie[6,7], Elizabeth M. Tennyson[1], Stuart Macpherson[1], Anna Abfalterer[1], Miguel Anaya[1,5], Yu-Hsien Chiang[1], Phillip Crout[4], Francesco Simone Ruggeri[8], Sean M. Collins[9], Clare P. Grey[2], Aron Walsh[3,10], Paul A. Midgley[4], Samuel D. Stranks[1,5]*

Efforts to stabilize photoactive formamidinium (FA)–based halide perovskites for perovskite photovoltaics have focused on the growth of cubic formamidinium lead iodide (α-$FAPbI_3$) phases by empirically alloying with cesium, methylammonium (MA) cations, or both. We show that such stabilized FA-rich perovskites are noncubic and exhibit ~2° octahedral tilting at room temperature. This tilting, resolvable only with the use of local nanostructure characterization techniques, imparts phase stability by frustrating transitions from photoactive to hexagonal phases. Although the bulk phase appears stable when examined macroscopically, heterogeneous cation distributions allow microscopically unstable regions to form; we found that these transitioned to hexagonal polytypes, leading to local trap-assisted performance losses and photoinstabilities. Using surface-bound ethylenediaminetetraacetic acid, we engineered an octahedral tilt into pure α-$FAPbI_3$ thin films without any cation alloying. The templated photoactive $FAPbI_3$ film was extremely stable against thermal, environmental, and light stressors.

Although early perovskite solar cells primarily used methylammonium (MA)–based absorber layers, formamidinium (FA)–based perovskites have much greater thermal stability. However, $FAPbI_3$ is challenging both to fabricate and stabilize, because the photoactive cubic phase (α-$FAPbI_3$) consisting of lead iodide octahedra is stable only at temperatures above 150°C, where it is entropically stabilized by the reorienting FA cations (*1*). At room temperature, the energy barrier is readily overcome and the material rapidly transitions to wide-bandgap, face-sharing hexagonal polytypes, such as the 2*H* δ-phase, 4*H*, or 6*H* phases (*2*, *3*). Alloying FA with Cs^+, MA, or both on the A-site cation of the ABX_3 perovskite structure can stabilize photoactive $FAPbI_3$-like cubic structures at room temperature. For example, perovskite solar cells fabricated with $Cs_{0.05}FA_{0.78}MA_{0.17}Pb(I_{0.83}Br_{0.17})_3$ (triple-cation) or those comprising $FAPbI_3$ alloyed with $MAPbBr_3$ perovskites have achieved high power conversion efficiencies (PCEs) with greatly enhanced reproducibility and ambient stability relative to pure $FAPbI_3$ (*4*–*8*). The most successful recent strategies for stabilizing pure $FAPbI_3$ perovskite thin films still incorporate a small fraction of alloying cations, including incorporation of MA through use of methylammonium chloride (in conjunction with formamidinium formate) (*9*), methylammonium thiocyanate vapor (*10*), methylammonium formate (*11*), or other cations such as Cs^+ and methylenediammonium (*12*, *13*).

These approaches lead recent record efficiency tables, and power conversion efficiencies have now exceeded 25.5% in single-junction and 29.5% in tandem configurations (*14*). Nonetheless, degradation to undesirable hexagonal by-products during the lifetime of a photovoltaic panel can still occur (*3*). Nanoscale domains of hexagonal-phase impurities can persist even in high-performing films that appear otherwise cubic in macroscopic measurements (*15*). These trace hexagonal domains induce clusters of deep trap states that are detrimental to performance (*16*, *17*) and induce photodegradation under operational conditions (*15*). Eliminating these hexagonal-phase impurities will be essential for commercial viability of these cells, but doing so requires a fundamental atomic-level understanding of why and how they form.

Improved cubic-phase stability has been attributed to tuning the Goldschmidt tolerance factor toward the perfect cubic perovskite structure through cation mixing (*7*, *18*), templating growth of the corner-sharing cubic structure (*10*, *11*), relaxing strain (*13*), or reducing intrinsic defect density (*9*). We found that stable, photoactive FA-rich perovskites exhibited small, symmetry-breaking, octahedral tilting at room temperature and actually have a noncubic structure. The magnitude of octahedral tilting is very small and only weak superstructure diffraction peaks are created that are below the noise threshold of traditional characterization techniques. We elucidated these features using local, low-dose, nanostructure probes and sensitive photon-counting detectors. This octahedral tilt–stabilized (ots) phase is induced through the alloying of cations and acts as an inherent photoactive material stabilizer by frustrating the transformation from the photoactive noncubic phase to hexagonal wide-bandgap phases. Although this alloying approach provides apparent phase purity if viewed macroscopically, spatial heterogeneity in cation distribution in the film is associated with local nanoscopic regions that are not tilted and thus form residual hexagonal-phase impurities (*15*, *17*).

We demonstrate a strategy in which surface-bound ethylenediaminetetraacetic acid (EDTA) templated the growth of ots-$FAPbI_3$ throughout the bulk film, as elucidated by solid-state nuclear magnetic resonance (NMR) and nuclear quadrupole resonance (NQR) measurements. The ots-$FAPbI_3$ films showed exceptional stability against thermal, atmospheric, and light stressors without any cationic additives.

We first solution-processed thin films of triple-cation $Cs_{0.05}FA_{0.78}MA_{0.17}Pb(I_{0.83}Br_{0.17})_3$ perovskite on SiN transmission electron microscope (TEM) substrates following a previously reported process (*16*). An electron diffraction (ED) pattern (maintaining low electron dose ~10 electrons/$Å^2$) extracted from a scanning ED (SED) measurement (*19*) of the film could in principle be indexed to a $[001]_c$ zone axis of the expected cubic perovskite $Pm\bar{3}m$ structure with a lattice parameter of ~6.3 Å (Fig. 1A) (*7*, *16*). However, in these SED scans with spatial resolution of 5 nm (extracted from individual grains 50 to 200 nm in size), very faint reflections, forbidden from appearing in the $Pm\bar{3}m$ space group, were visible (Fig. 1A, white arrows). The same forbidden reflections were also observed in measurements from many different sample batches and experimental measurements, as well as in analogous pure-iodide $Cs_{0.05}FA_{0.78}MA_{0.17}PbI_3$ thin films (fig. S1). Thus, these triple-cation compositions, regardless of halide composition, have a noncubic structure.

We attributed these superstructure reflections to octahedral tilting whereby the BX_6 corner-sharing octahedra tilt away from perfect cubic symmetry into 1 of 15 lower symmetry

[1]Department of Physics, Cavendish Laboratory, University of Cambridge, Cambridge, UK. [2]Yusuf Hamied Department of Chemistry, University of Cambridge, Cambridge, UK. [3]Department of Materials Science and Engineering, Yonsei University, Seoul, Korea. [4]Department of Materials Science and Metallurgy, University of Cambridge, Cambridge, UK. [5]Department of Chemical Engineering and Biotechnology, University of Cambridge, Cambridge, UK. [6]Electron Physical Science Imaging Centre, Diamond Light Source Ltd., Didcot, UK. [7]Department of Materials, University of Oxford, Oxford, UK. [8]Laboratories of Organic and Physical Chemistry, Wageningen University and Research, Wageningen, Netherlands. [9]School of Chemical and Process Engineering and School of Chemistry, University of Leeds, Leeds, UK. [10]Department of Materials, Imperial College London, London, UK.
*Corresponding author. Email: sds65@cam.ac.uk
†These authors contributed equally to this work.

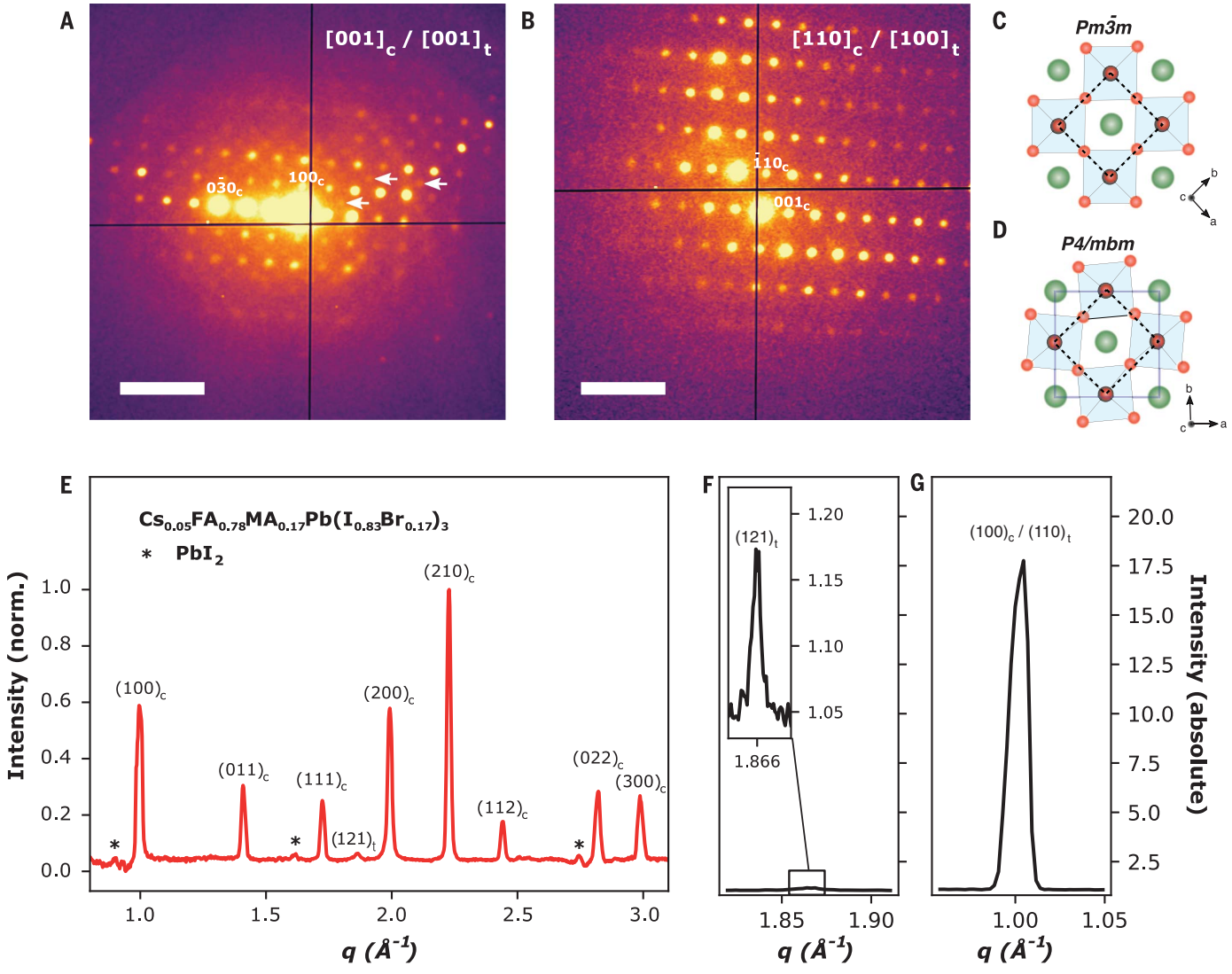

Fig. 1. Structural identification of tetragonal $Cs_{0.05}FA_{0.78}MA_{0.17}Pb(I_{0.83}Br_{0.17})_3$ thin films. (**A**) The ED pattern of a $Cs_{0.05}FA_{0.78}MA_{0.17}Pb(I_{0.83}Br_{0.17})_3$ sample oriented near the [001] zone axis of a cubic unit cell ($[001]_c$) or the $[001]_t$ zone axis of a tetragonal unit cell. The superstructure reflections indicated by white arrows are forbidden from appearing in a cubic structure. (**B**) The ED pattern of a $Cs_{0.05}FA_{0.78}MA_{0.17}Pb(I_{0.83}Br_{0.17})_3$ film oriented near the $[110]_c$/$[100]_t$ zone axis. Superstructure reflections are absent. (**C**) Schematic representation of the cubic *Pm*$\bar{3}$*m* perovskite structure viewed along the $[001]_c$ direction. Green spheres represent A-site cations; red spheres represent halides. B-site cations are represented by gray spheres that are partially visible and are enclosed in blue octahedral cages. The cubic unit cell is indicated by a black dashed box. (**D**) Schematic representation of the tetragonal *P4/mbm* perovskite structure viewed along $[001]_c$. The tetragonal unit cell is indicated by the blue box connecting A-site cations. The pseudo-cubic unit cell is indicated by a black dashed box. (**E**) Mean nano–x-ray diffraction (nXRD) pattern of a $Cs_{0.05}FA_{0.78}MA_{0.17}Pb(I_{0.83}Br_{0.17})_3$ thin film extracted by spatially averaging across a 15 μm × 10 μm region. The pattern was normalized between 0 and 1 by subtracting the minimum value and scaling with the maximum value from the respective map of peak intensity ratio. (**F**) $(121)_t$ tetragonal XRD peak extracted from local nXRD measurements. Inset: Close-up of $(121)_t$ peak. (**G**) $(100)_c$/$(110)_t$ XRD peak extracted from local nXRD measurements. Note that (F) and (G) are plotted on the same intensity scale. Scale bars, 0.5 $Å^{-1}$ [(A) and (B)].

space groups (fig. S2) (*20*). We exclude the possibility that the superstructure reflections could be attributed to effects other than octahedral tilting, such as dynamical scattering, or cation ordering (see text S1). We also exclude the possibility that electron beam-induced structural changes affected the interpretation of our results as our measurements were acquired over an order of magnitude below the electron doses at which beam-induced effects are observed. We also observed these superstructure reflections in halide perovskite compositions known to possess a tilted, noncubic, structure (*21*, *22*) [fig. S3; see also (*19*) and text S1].

Interrogating superstructure reflections at particular orientations allows the unambiguous assignment of space groups from ED patterns of octahedrally tilted perovskites (*20*), and is typically achieved by tilting a single crystalline sample into different orientations and recording an ED pattern at each orientation. However, this methodology is not compatible with the most technologically relevant halide perovskite materials given their polycrystalline nature, small grains, and beam sensitivity. We used the low-dose, large-area scanning capabilities of SED to sample many individual grains at orientations other than $[001]_c$ and determine the actual symmetry of the FA-rich alloyed (triple-cation) perovskite unit cell.

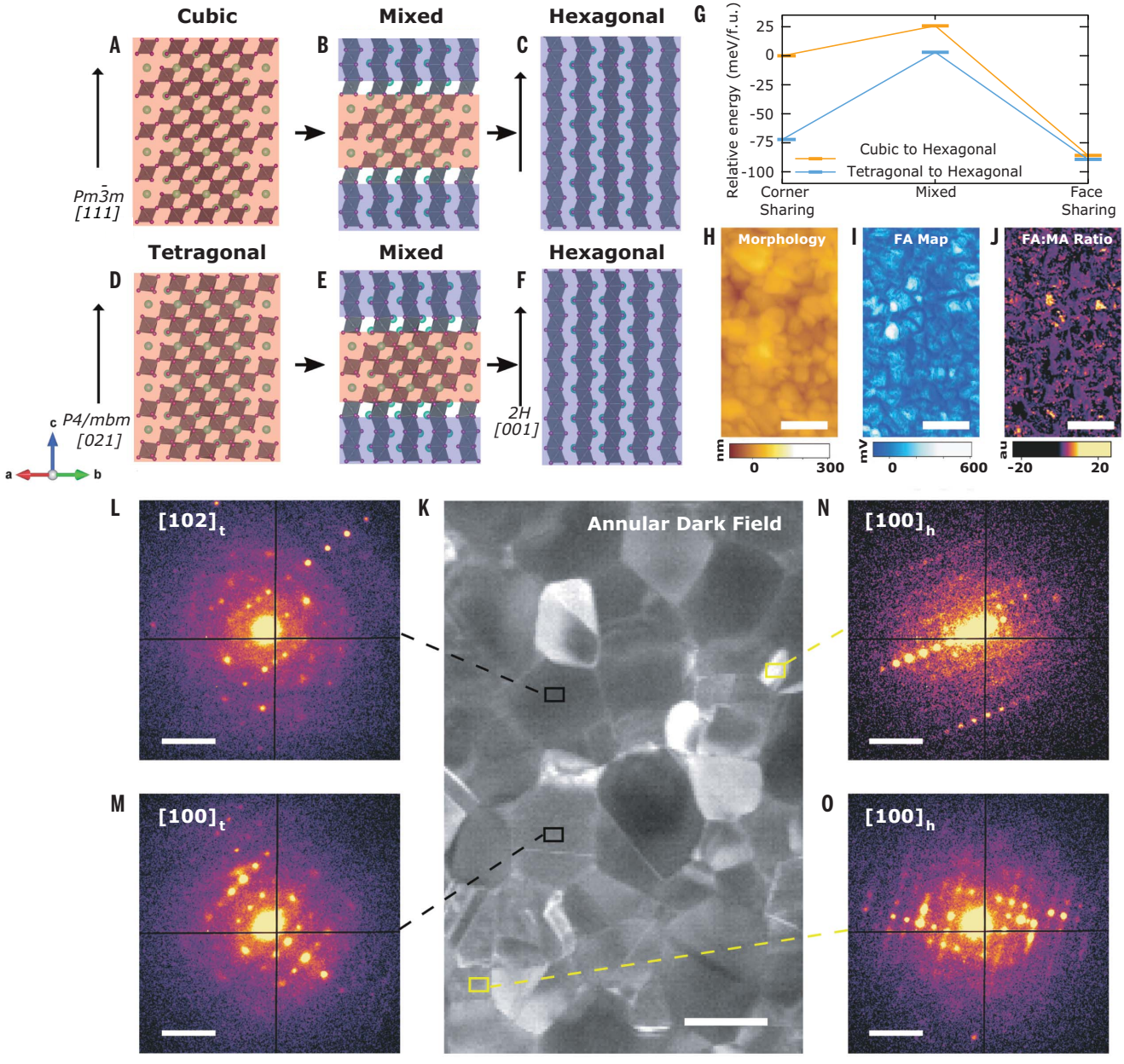

Fig. 2. Tilted octahedra stabilize photoactive perovskites against degradation. (**A** to **C**) Progression of the structural transition from the corner-sharing cubic $Pm\bar{3}m$ structure (A) to the *2H* hexagonal face-sharing structure (C) by way of a mixed corner-sharing and face-sharing intermediary structure (B). (**D** to **F**) Progression of the structural transition from the corner-sharing tetragonal *P4/mbm* structure (D) to the *2H* hexagonal face-sharing structure (F) by way of a mixed corner-sharing and face-sharing intermediate structure (E). (**G**) Relative energy difference between the corner-sharing, mixed, and face-sharing phases for the cubic-to-hexagonal (gold) and tetragonal-to-hexagonal (blue) transition. (**H** and **I**) For a $Cs_{0.05}FA_{0.78}MA_{0.17}Pb(I_{0.83}Br_{0.17})$ thin film, AFM-IR morphology map (H) and IR absorption maps of the FA content (I) (peak at 1712 cm^{-1}). (**J**) IR chemical ratio of the FA:MA cation distribution extracted by dividing the IR map of FA content in (I) by the IR map of MA content in fig. S8. (**K**) Annular dark-field image reconstructed from SED data of a region of a $Cs_{0.05}FA_{0.78}MA_{0.17}Pb(I_{0.83}Br_{0.17})_3$ thin film. Hexagonal phase impurities are shaded in yellow. (**L** and **M**) ED patterns extracted from a black region of interest in (K), revealing a grain oriented near the $[102]_t$ zone axis (L) and a grain oriented near the $[100]_t$ zone axis (M). (**N** and **O**) ED patterns of the yellow boxed region of interest shown in (K), revealing a *2H* hexagonal phase impurity oriented near the $[100]_h$ zone axis (N) and oriented near the $[100]_h$ zone axis (O). Scale bars, 800 nm [(H) to (J)], 200 nm (K), 0.5 $Å^{-1}$ [(L) to (O)].

Group-subgroup relations (fig. S2), along with the symmetry of the experimentally observed superstructure reflections for triple-cation samples, indicated that the most likely space groups were either tetragonal *P4/mbm* or orthorhombic *Pnma* (*20*, *23*). However, the ED pattern of grains oriented near a $\langle 110 \rangle_c$ zone axis (Fig. 1B and figs. S4 to S6) revealed no superstructure reflections when compared to the expected cubic structure. In the *Pnma* space group, superstructure reflections are expected in 2 of 12 $\langle 110 \rangle_c$ zone axis diffraction patterns, whereas in the *P4/mbm* space group, they are expected in none (fig. S4) (*20*). The persistent absence of these reflections in our

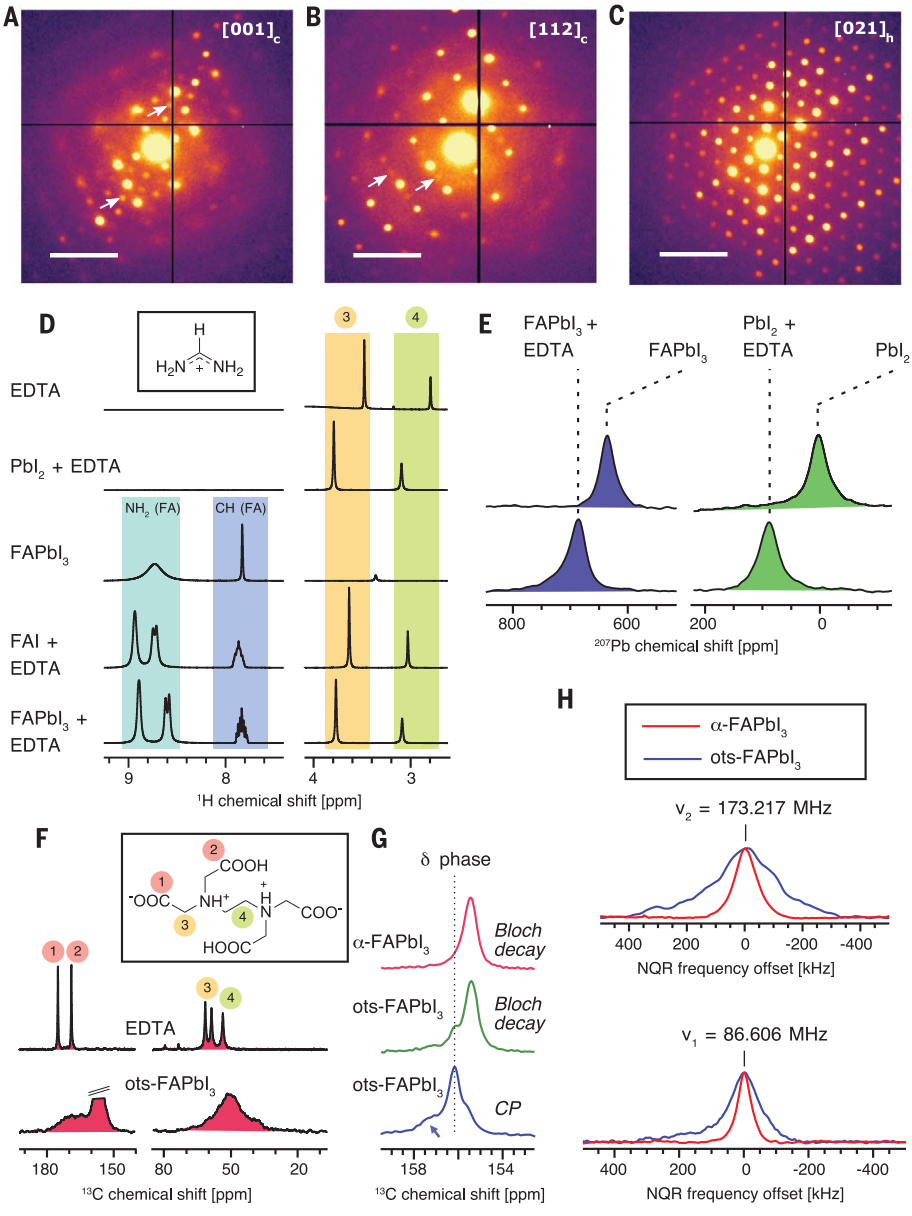

Fig. 3. Surface-bound ethylenediaminetetraacetic acid (EDTA) templates growth of octahedral tilt–stabilized (ots)-$FAPbI_3$. (**A** and **B**) The SED pattern for ots-$FAPbI_3$ perovskite thin films near the $[001]_c$ zone axis (A) and near the $[112]_c$ zone axis (B). A subset of superstructure reflections is highlighted with white arrows in each SED pattern. (**C**) The SED pattern for a hexagonal (6*H*) structure present in the ots-$FAPbI_3$ perovskite thin film oriented near the [021] zone axis. (**D**) Liquid-state ^{1}H NMR of the precursor solution reveals that EDTA interacts with Pb^{2+} ions (in mixtures with PbI_2 and $FAPbI_3$) and FA ions (in mixtures with FAI and $FAPbI_3$). The protonation of FA by EDTA hinders the rotation around the partial double C–N bonds, rendering the two protons within the two NH_2 moieties inequivalent (visible via the peak splitting of the FA NH_2 resonances and the J-coupling on both the FA CH and NH_2 resonances). The inset shows the structure of protonated FA. (**E**) Liquid state ^{207}Pb NMR corroborates the Pb^{2+}-EDTA interaction in the precursor solution of dissolved PbI_2 and $FAPbI_3$. (**F**) ^{1}H-^{13}C CP MAS NMR reveals that EDTA in EDTA-doped $FAPbI_3$ (scraped-off material from drop-cast films) is substantially disordered relative to neat EDTA. The intense peak of FA environments is clipped here for clarity. The inset shows the structure of EDTA. (**G**) The "FA" region of the Bloch decay–detected (i.e., pulse-acquire) ^{13}C MAS NMR spectrum (green) shows that most of the FA environments are unchanged in ots-$FAPbI_3$ and correspond to FA within α-$FAPbI_3$. New environments are also present that correspond to δ-$FAPbI_3$ as well as FA interacting with EDTA (indicated by an arrow in the CP spectrum, blue). (**H**) ^{127}I nuclear quadrupole resonance (NQR) spectra of α-$FAPbI_3$ and ots-$FAPbI_3$ reveal more asymmetric local structure of iodides in the latter material. We attribute this effect to a reduction in overall crystallographic symmetry as a result of structure templating by the surface-bound EDTA. Scale bars, 0.7 $Å^{-1}$ [(A) to (C)].

experimentally observed $\langle 110 \rangle_c$ zone axis patterns thus provides strong evidence that these triple-cation perovskites had a tetragonal *P4/mbm* structure.

The weak nature of the superstructure reflections observed here, which were resolvable with SED given that the interaction of electrons with matter is orders of magnitude stronger than that of x-rays, suggested that the structural deviation from cubic (Fig. 1, C and D) is very small and would be extremely difficult to detect in laboratory Bragg x-ray diffraction (XRD) [see (*19*)], and was consistent with previous assignments of the triple-cation perovskite to a cubic structure (*7*). We used synchrotron-based nano XRD (nXRD) experiments to quantify the degree of octahedral tilting present in FA-rich alloyed samples. A 50-nm focused x-ray probe allowed us to scan local regions of a sample, acquiring both single-crystal patterns from individual grains and powder patterns representative of the bulk of the material by spatially averaging across every probe position in a given scan. Even with monochromated synchrotron light and a highly sensitive photon-counting detector (*19*), we only observed weak diffracted intensity from the $(121)_t$ tetragonal superstructure reflection in a spatially averaged nXRD pattern across a 15 μm × 10 μm region of a triple-cation film sample (Fig. 1E) (*19*). All other tetragonal superstructure peaks had an intensity below or comparable to the noise of the averaged pattern.

However, the local nature of nXRD allowed us to use virtual dark-field imaging (fig. S7) (*19*) to exclusively extract regions in the scan where the Bragg condition was satisfied for tetragonal superstructure peaks. This approach substantially increased the signal-to-noise ratio, allowed extraction of local tetragonal superstructure peaks (Fig. 1F and inset), and mitigated the impact of local film texture on the analysis of diffracted intensity. As the intensity of superstructure peaks relative to primary Bragg peaks is directly related to the degree of octahedral tilting (*24*), we could compare the averaged intensities *I* of the tetragonal $(121)_t$ Bragg peak (Fig. 1F) to the much stronger primary $(100)_c/(110)_t$ Bragg peak (Fig. 1G) to show that $I_{(121)t}$ was 0.75% of $I_{(100)c/(110)t}$. A comparison of this relative intensity to kinematical simulations of a range of different octahedral tilt angles indicated an octahedral rotation in the range 0.75° to 2.75° about the c axis of the

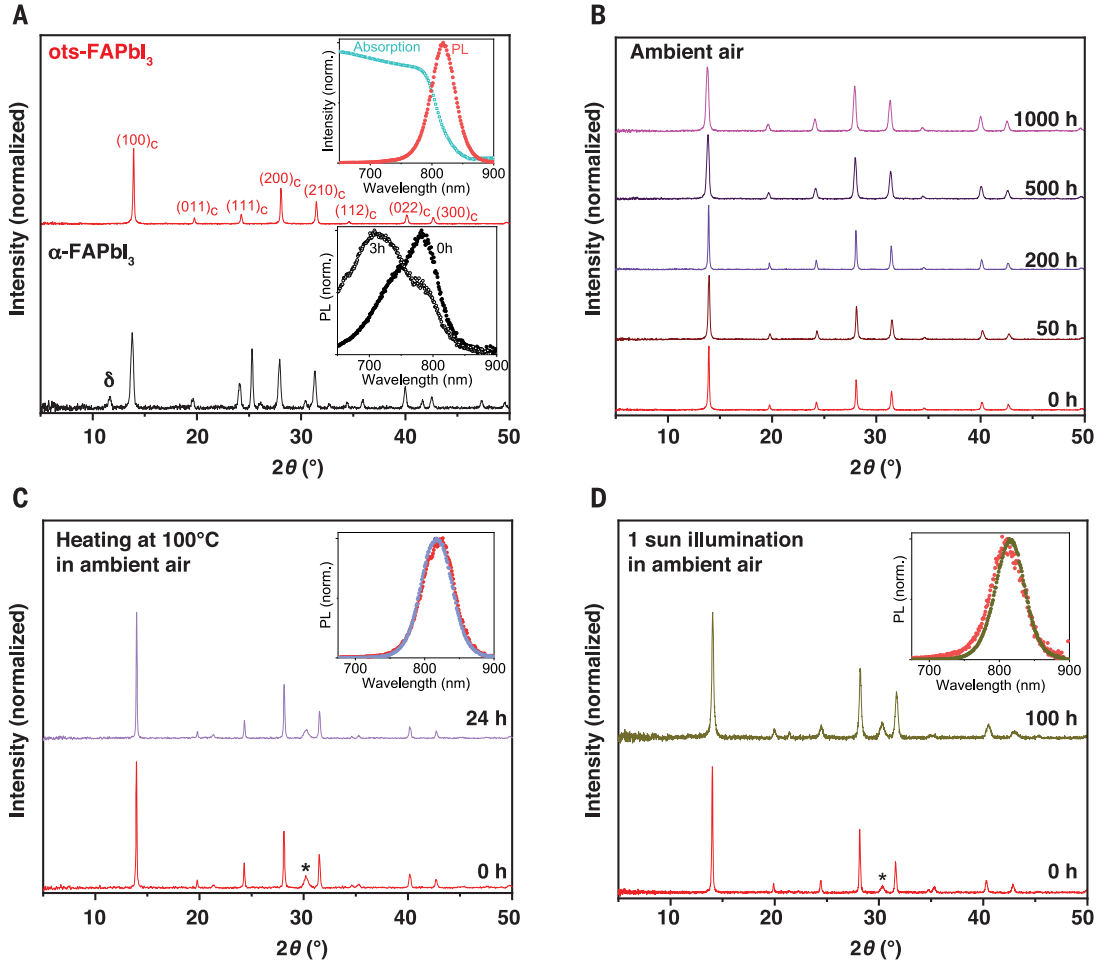

Fig. 4. ots-$FAPbI_3$ perovskite films are highly stable against atmospheric, thermal, and light stressors. (**A**) X-ray diffraction (XRD) pattern for a control α-$FAPbI_3$ sample (bottom pattern, black) taken immediately after exposing to ambient air, with a δ-phase peak already present. The inset shows PL spectra of a film taken initially (0 hours corresponds to ~5 min of total exposure to ambient air) and again after 3 hours of exposure. Note that these control α-$FAPbI_3$ films are rapidly degrading during the measurements in ambient air, and thus these spectra are merely snapshots in time of the samples during the degradation. The top pattern (red) shows the XRD pattern of an ots-$FAPbI_3$ film, indexed to the cubic structure for labeling purposes, with no signature of additional phase impurities. The inset shows the corresponding absorption (open blue symbols) and PL (solid red symbols) spectra of the film. (**B**) XRD pattern of an ots-$FAPbI_3$ film stored in ambient air over a period of 1000 hours, showing negligible change. (**C**) XRD pattern of an ots-$FAPbI_3$ film subjected to continuous heating at 100°C for 24 hours in ambient air, showing very little change. The inset shows that the PL spectra also exhibit minimal change after the heating. (**D**) XRD pattern of an ots-$FAPbI_3$ film subjected to continuous illumination under 1-sun intensity (AM1.5) for 100 hours in ambient air, showing only small changes in patterns. The inset shows that the PL spectra also exhibit minimal change after the illumination, other than a small spectral narrowing. Asterisk in (C) and (D) denotes peak from the ITO substrate.

unit cell (Fig. 1D) [see fig. S7, (*19*), and text S2 for calculation of relative peak intensity, estimation of octahedral rotation and its range, and extraction of local diffraction data]. Our collective results revealed that these FA-rich alloyed cation compositions intrinsically had small octahedral tilting structural distortions that were not observable in macroscopic Bragg diffraction experiments but resolvable by the local Bragg diffraction measurements used here.

The crystallization of FA-rich alloyed perovskites in this slightly tilted, corner-sharing, photoactive phase at room temperature was surprising. We hypothesize that the ots phase led to reported improved stability and resistance to transforming into the hexagonal phases when compared to untreated cubic α-$FAPbI_3$ (*25*). To test whether the tilted octahedra of the tetragonal *P4/mbm* triple-cation perovskite provided an innate barrier to forming a hexagonal face-sharing structure, we probed the thermodynamics of the transformation between corner and face-sharing octahedral networks using first-principles density functional theory (DFT) total energy calculations [see (*19*)]. We considered both the cubic $Pm\bar{3}m$ phase (Fig. 2A) and the tetragonal *P4/mbm* (Fig. 2D) as the starting corner sharing phases and the same hexagonal 2*H* phase as the final face-sharing phase (Fig. 2, C and F). The energy difference (thermodynamic driving force) between the cubic and hexagonal phases was 86 meV (Fig. 2G), whereas the difference between the tetragonal and hexagonal phase was only 17 meV.

We estimated the thermodynamic cost to form a mixed corner/face-sharing phase (Fig. 2B for cubic and Fig. 2E for tetragonal), which is an intermediate between the corner-sharing and face-sharing phases. These values provided a lower bound for the phase transition barrier: We obtain a barrier height of 26 meV per formula unit for the cubic-to-hexagonal phase transition and 75 meV/f.u. for the tetragonal-to-hexagonal phase transition, again indicating that the cubic phase was more susceptible to transitioning to hexagonal polytypes. We note that the phase transition may be further influenced by reorientations of the organic cation (*26*). Although transitions between cubic corner-sharing and hexagonal face-sharing structures are well documented in halide perovskites, oxide perovskites, and silicon carbide materials (*27*–*29*), the same is not true for tetragonal corner-sharing (or other tilted structures) to hexagonal face-sharing transitions.

Given we observed the tetragonal structure in both mixed halide and single halide FA-rich alloyed cation compositions (Fig. 1, A and B, and fig. S1), and that the structurally similar α-$FAPbI_3$ had an average cubic structure at room temperature, as revealed by neutron diffraction experiments (*25*), we propose that room-temperature octahedral tilting in FA-rich perovskites originated primarily from alloying of the FA, Cs^+, or MA cations (or some combination) on the A-site. Specifically, the

mixing of different-sized cations induced a small distortion of the perovskite's local unit cell that frustrated the structural transformation to 2*H* and other hexagonal phases. We note that halide mixing could additionally influence the observed degree of octahedral tilting (fig. S8 and text S1) (*19*).

Using atomic force microscopy–based infrared nanospectroscopy (AFM-IR) to simultaneously map the morphology of the film (Fig. 2H) and the spatial distribution of the chemical signature of the FA (at 1712 cm^{-1}; Fig. 2I) and MA (1466 cm^{-1}; fig. S8) of a triple-cation perovskite thin film, we observed discrete FA-rich regions of the film ~50 to 200 nm in size, as seen in the FA:MA ratio map in Fig. 2J (see also fig. S9) (*30*). SED measurements (Fig. 2K) revealed that although most of the film exhibited *P*4/*mbm* symmetry (Fig. 2, K to M), we also observed discrete inclusions indexable to hexagonal polytype structures ~50 to 150 nm in size and comparable to the length scales of the FA-rich domains (Fig. 2, K, N, and O; see fig. S10 for additional examples).

On the basis of these observations, we concluded that these hexagonal regions were linked to the heterogeneity in the cation distribution. For example, regions of the film with a local excess of FA, such as those visualized by AFM-IR (Fig. 2, I and J), had a reduced content of Cs^+, MA, or both (Fig. 2, J and K, and fig. S9). The locally higher FA content allowed hexagonal phases to form either directly during the crystallization process (which cation alloying would otherwise have inhibited) (*2*, *31*), or indirectly after annealing as the FA-rich environment favored the formation of the photoactive perovskite as a cubic $Pm\bar{3}m$ structure rather than a tetragonal *P4/mbm* structure. The cubic structure then readily transformed to 2*H* and other hexagonal phases.

Even if these phases appear stabilized when probed macroscopically through small additions of other cations (*2*, *32*), typically used film-processing approaches for devices can leave phase impurities that persist on the nanoscale (in general unobservable in macroscopic techniques) (*16*, *17*) and induce degradation under operation (*15*). The pathway to highly stable and efficient FA-rich perovskite devices is through the slight distortion of octahedra across the sample to a degree that frustrates the transition from corner-sharing to face-sharing structures but does not compromise optoelectronic properties for example by widening the bandgap or reducing carrier lifetimes (*33*). To selectively induce octahedral tilt in $FAPbI_3$ at room temperature without alloying multiple A-site cations, we used ethylenediaminetetraacetic acid (EDTA) as an additive to the precursor solution of $FAPbI_3$ (*19*), considering the potential for such bifunctional molecules to interact with both Pb^{2+} ions and ammonium cations in precursor solutions, during film formation, or both. We spin-coated EDTA-containing perovskite precursors on substrates that were then annealed at 150°C for 1 hour in a nitrogen glove box to form a visibly stable, optically active film of the black perovskite phase (see fig. S11 for optimization of EDTA concentration). We did not include any other additives, which allowed us to study the pure $FAPbI_3$ systems.

SED patterns extracted from the resulting perovskite thin films (Fig. 3, A and B) confirmed the presence of superstructure reflections identical to those observed in the *P*4/*mbm* FA-rich perovskites, indicating that octahedral tilting occurred in the fabricated $FAPbI_3$. Occasionally, superstructure reflections inconsistent with *P*4/*mbm* symmetry were observed (fig. S12), which suggested that multiple octahedral tilt systems were present that we were unable to unambiguously assign. Notably, in each place that we observed a corner-sharing photoactive perovskite structure, we also observed octahedral tilting in ots-$FAPbI_3$. Furthermore, in the infrequent local regions where octahedral tilting was not observed, hexagonal-phase impurities were present (Fig. 3C). These results provided further support for our assertion that octahedral tilt is critical for minimizing the formation of such phase impurities.

To elucidate the microscopic mechanism of the EDTA-induced stabilization of $FAPbI_3$, we performed NMR experiments to probe local structure (*34*, *35*). ^{1}H liquid-state NMR of the precursor solutions showed a prominent shift of the acetate and ethylenic CH_2 groups of EDTA, added in the neat acid form (*36*), in the presence of dissolved PbI_2 at $\Delta\delta$ = +0.3 parts per million (ppm) and $FAPbI_3$ at $\Delta\delta$ = +0.3 ppm (Fig. 3D). Although EDTA is a strong chelator, we did not observe the formation of a long-lived, hexadentate Pb-EDTA chelate that would lead to splitting of the acetate methylene protons (see text S3) (*37*). We attributed the relative shifts to a combination of changes in the protonation equilibrium because EDTA can exist in six forms with different protonation levels, and a shorter-lived or more disordered Pb^{2+}-EDTA complex. Additional proof of the Pb^{2+}-EDTA interaction was provided by the relative shift in ^{207}Pb NMR spectra of the precursor solutions when EDTA is added (Fig. 3E). In addition, EDTA protonates the FA moiety, hindering the C–N bond rotation, as indicated by the appearance of a set of signals associated with the two inequivalent NH_2 groups of FA and the corresponding CH multiplet (*38*).

We next investigated ots-$FAPbI_3$ by solid-state NMR. ^{207}Pb and ^{14}N solid-state NMR spectra of scraped-off material from drop-cast films showed that the perovskite component of ots-$FAPbI_3$ was virtually identical to that of control α-$FAPbI_3$, within the sensitivity of these two techniques (fig. S13). ^{13}C solid-state NMR allowed us to elucidate the speciation of EDTA in the ots-$FAPbI_3$ material (Fig. 3F). Although neat crystalline EDTA is characterized by narrow ^{13}C resonances [full width at half maximum (FWHM) = 0.3 to 0.9 ppm], the FWHM of both the carbonyl and methylene carbons in ots-$FAPbI_3$ was 14 to 15 ppm, indicating that the EDTA was in an amorphous phase (or component). The ^{13}C resonances of FA revealed that there were multiple FA-containing local environments. Although the largest component corresponded to the three-dimensional perovskite phase of ots-$FAPbI_3$, there was also a smaller component corresponding to the residual δ-phase, consistent with the presence of small fractions of hexagonal polytypes in the SED data (Fig. 3C).

We also detected another substantially broader FA peak corresponding to a more disordered FA local environment, which we attribute to the interfacial FA ions of the perovskite phase interacting directly with EDTA (Fig. 3G, arrow). Cross-polarization (CP) indicates that the local environment was rigid and not undergoing rapid near-isotropic reorientation characteristic for FA inside the A-site cation cage. ^{14}N NMR is highly sensitive to changes in lattice symmetry induced by incorporation of additives into the perovskite structure (*35*). The ^{14}N spectrum of the fast-reorienting FA inside a 3D perovskite cage (fig. S13) showed that the symmetries of ots-$FAPbI_3$ and control α-$FAPbI_3$ are essentially identical within the sensitivity of this approach, indicating that the EDTA did not incorporate into the perovskite structure.

To elucidate the much smaller effect of EDTA on the lattice symmetry, we used ^{127}I NQR. In NQR, the nuclear energy levels are split by the electric field gradient (EFG) around the nucleus and not by an external magnetic field, as in NMR (fig. S13). The resulting transitions can be driven at specific frequencies that depend on the magnitude of the EFG, which is determined by local symmetry. The NQR spectrum of the control α-$FAPbI_3$ sample contained two signals corresponding to the ±3/2 ⟷ ±5/2 and ±1/2 ⟷ ±3/2 transitions of the ^{127}I nucleus at 173.217 and 86.606 MHz, with FWHM of 87 and 47 kHz, respectively (Fig. 3H). The broadening of the ^{127}I NQR resonances in ots-$FAPbI_3$ (FWHM = 246 and 112 kHz for ±3/2 ⟷ ±5/2 and ±1/2 ⟷ ±3/2, respectively) evidenced that there was a broader distribution of local iodide environments compared to the control α-$FAPbI_3$. This result was consistent with the resulting octahedrally tilted phase having lower symmetry.

In a tetragonal $FAPbI_3$, each of the two NQR resonances present in cubic $FAPbI_3$ would split into two because there are two crystallographically inequivalent iodide sites in the unit cell of tetragonal $FAPbI_3$ (*39*). Splitting was not observed here, indicating that the

degree of distortion is characterized by a distribution rather than a clear-cut value throughout the material, consistent with SED observations of multiple local octahedral tilting symmetries (fig. S12). The FWHM of the $\pm 3/2 \leftrightarrow \pm 5/2$ transition of ots-$FAPbI_3$ (246 kHz) corresponds to the maximum degree of distortion present in neat tetragonal β-$FAPbI_3$ at ~280 K (*40*). Notably, ^{14}N NMR (fig. S13), which has recently been used to show that the symmetry of A-site cation cages of $FAPbI_3$ increases when it is stabilized with methylammonium thiocyanate (*10*), was not sensitive enough to detect the minor deviations from cubic symmetry identified here by NQR, SED, and nXRD (text S4).

Taken together, these results show that we induced octahedral distortion in the material through a structure-directing effect of EDTA, with the EDTA binding to the $FAPbI_3$ surface but not incorporating into the $FAPbI_3$ structure. We expect that this will spur further experimental and computational work to establish the exact binding modes of EDTA, identify other growth-templating additives, and understand their effect on crystallization and the resulting spatial variation of the tilt.

We examined octahedral tilt stabilization of the $FAPbI_3$ films by subjecting them to a variety of external stressors. The bulk XRD pattern of the ots-$FAPbI_3$ film (Fig. 4A, red) could in principle be indexed to a $Pm\bar{3}m$ cubic structure, despite possessing a lower-symmetry tilted structure (see Fig. 3, A and B), as the superstructure reflections arising from octahedral tilting were below the detection limit of bulk XRD measurements. There was no macroscopic evidence for phase impurities, despite trace amounts on the nanoscale (see Fig. 3C), consistent with the clean absorption and photoluminescence (PL) spectra observed (Fig. 4A, top inset). However, the control α-$FAPbI_3$ films showed the macroscopic presence of the 2*H* δ-phase after only ~5 min (time required to load and measure the sample) of air exposure (XRD peak at 11.6°; Fig. 4A, black), together with an asymmetric PL peak (Fig. 4A, inset; see fig. S14 for cleaner PL spectra of encapsulated control samples). Furthermore, the PL lifetime of the control α-$FAPbI_3$ film was reduced by a factor of 4 with respect to an ots-$FAPbI_3$ film (fig. S14), consistent with the phase impurities in the control films acting as nonradiative recombination centers (*17*). Exposure of the control film to ambient air for 3 hours caused the PL spectral shape and position to change rapidly and substantially (Fig. 4A, bottom inset). These changes were concomitant with further growth of the intensity of the 2*H* δ-phase peak (fig. S15).

After 1000 hours in ambient air, XRD patterns of the ots-$FAPbI_3$ films did not show any macroscopic conversion to hexagonal phases (Fig. 4B), and we observed the presence of impurity phases only after 1500 hours of air exposure (fig. S16). Furthermore, we observed similar phase stability when heating the ots-$FAPbI_3$ perovskite films in ambient air for 24 hours at 100°C, with negligible change in the XRD pattern (Fig. 4C; similar results in nitrogen, fig. S17) or PL spectra (Fig. 4C, inset) after this extended heating. After continuous illumination of the ots-$FAPbI_3$ film under 1-sun (AM1.5) intensity for 100 hours in ambient air, there were no phase impurities evident in XRD (Fig. 4D) or sizable changes observed in PL spectra (Fig. 4D, inset) other than a slight narrowing of the peak and a very slight redshift, the origin of which is currently unclear. The PL properties of the ots-$FAPbI_3$ films were actually enhanced after the heating and illumination tests: The PL lifetimes reached 83 ns after the heating (fig. S18) and 592 ns after the illumination (fig. S19), consistent with light- and oxygen-assisted passivation reported previously for halide perovskites (*40*). These combined results show the resilient stabilizing effect against the generation of impurity phases that the octahedral tilting imparts to photoactive FA-rich perovskites, even for bare films in ambient air under rigorous external stressors.

We have shown that the intrinsic stabilization mechanism of FA-rich mixed-cation systems is an octahedral tilt induced by cation alloying. This octahedral tilting is so minor (~2°) as to be undetectable with bulk characterization techniques yet, remarkably, frustrates the transformation from photoactive, tilted perovskite phases to wide-bandgap, performance-limiting hexagonal polytypes (e.g., the 2*H* δ-phase). We propose that the recent reports of stabilized cubic α-$FAPbI_3$, which have produced devices that are leading the efficiency tables and make use of constituent cations and other additives to improve stability, serendipitously benefit from this same minor octahedral tilting (*9*–*13*). However, homogeneously inducing a tilted structure through cation alloying across a perovskite film is already challenging at lab scale and will only become more so at commercial scale. Any local regions (even trace amounts) of a fabricated FA-rich perovskite that do not possess a tilted structure and are thus cubic will more readily transform to hexagonal phases, which generates nonabsorbing material as well as deep traps and photodegradation pathways under operation (*15*, *17*).

Developing new strategies that can work both in conjunction with cation-alloying approaches and independently of them to homogenize nanoscale phase stability and eliminate residual traps will be critical to realize single-junction and tandem perovskite photovoltaics operating near their performance limits throughout their commercial life cycle (*41*). This is especially true for the most promising compositions for single-junction commercialization, such as α-$FAPbI_3$, where cationic additives produce unwanted shifts to higher bandgap and compromise thermal stability (*6*, *7*, *9*). Here, we have outlined key guidelines for achieving this, by templating the growth of octahedral tilting through additives that do not incorporate into the perovskite structure, such as EDTA, without the use of additional A-site cations.

REFERENCES AND NOTES

1. T. Chen *et al.*, *Sci. Adv.* **2**, e1601650 (2016).
2. P. Gratia *et al.*, *ACS Energy Lett.* **2**, 2686–2693 (2017).
3. P. E. Marchezi *et al.*, *J. Mater. Chem. A* **8**, 9302–9312 (2020).
4. W. S. Yang *et al.*, *Science* **348**, 1234–1237 (2015).
5. W. S. Yang *et al.*, *Science* **356**, 1376–1379 (2017).
6. N. J. Jeon *et al.*, *Nature* **517**, 476–480 (2015).
7. M. Saliba *et al.*, *Energy Environ. Sci.* **9**, 1989–1997 (2016).
8. T. Bu *et al.*, *Science* **372**, 1327–1332 (2021).
9. J. Jeong *et al.*, *Nature* **592**, 381–385 (2021).
10. H. Lu *et al.*, *Science* **370**, eabb8985 (2020).
11. W. Hui *et al.*, *Science* **371**, 1359–1364 (2021).
12. H. Min *et al.*, *Science* **366**, 749–753 (2019).
13. G. Kim *et al.*, *Science* **370**, 108–112 (2020).
14. NREL, Best Research-Cell Efficiency Chart (2021); www.nrel.gov/pv/cell-efficiency.html.
15. S. Macpherson *et al.*, Local Nanoscale Defective Phase Impurities Are the Sites of Degradation in Halide Perovskite Devices. arXiv 2107.09549 [cond-mat] (20 July 2021).
16. T. A. S. Doherty *et al.*, *Nature* **580**, 360–366 (2020).
17. S. Kosar *et al.*, *Energy Environ. Sci.* 10.1039/D1EE02055B (2021).
18. J. Y. Kim, J.-W. Lee, H. S. Jung, H. Shin, N.-G. Park, *Chem. Rev.* **120**, 7867–7918 (2020).
19. See supplementary materials.
20. D. I. Woodward, I. M. Reaney, *Acta Crystallogr. B* **61**, 387–399 (2005).
21. R. E. Beal *et al.*, *Matter* **2**, 207–219 (2020).
22. S. Chen *et al.*, *Nat. Commun.* **9**, 4807 (2018).
23. R. dos Reis *et al.*, *Appl. Phys. Lett.* **112**, 071901 (2018).
24. G. O. Jones, P. A. Thomas, *Acta Crystallogr. B* **58**, 168–178 (2002).
25. M. T. Weller, O. J. Weber, J. M. Frost, A. Walsh, *J. Phys. Chem. Lett.* **6**, 3209–3212 (2015).
26. E. M. Mozur *et al.*, *Chem. Mater.* **29**, 10168–10177 (2017).
27. L. S. Ramsdell, *Am. Mineral.* **32**, 64–82 (1947).
28. C. C. Stoumpos, C. D. Malliakas, M. G. Kanatzidis, *Inorg. Chem.* **52**, 9019–9038 (2013).
29. S. Fop *et al.*, *Nat. Mater.* **19**, 752–757 (2020).
30. R. Szostak *et al.*, *Sci. Adv.* **5**, eaaw6619 (2019).
31. H. T. Pham *et al.*, *Nano Energy* **87**, 106226 (2021).
32. H. X. Dang *et al.*, *Joule* **3**, 1746–1764 (2019).
33. R. Prasanna *et al.*, *J. Am. Chem. Soc.* **139**, 11117–11124 (2017).
34. L. Piveteau, V. Morad, M. V. Kovalenko, *J. Am. Chem. Soc.* **142**, 19413–19437 (2020).
35. D. J. Kubicki, S. D. Stranks, C. P. Grey, L. Emsley, *Nat. Rev. Chem.* **5**, 624–645 (2021).
36. S. Aime, R. Gobetto, R. Nano, E. Santucci, *Inorg. Chim. Acta* **129**, L23–L25 (1987).
37. E. Hafer *et al.*, *Magn. Reson. Chem.* **58**, 653–665 (2020).
38. W. T. M. Van Gompel *et al.*, *J. Phys. Chem. C* **122**, 4117–4124 (2018).
39. K. Yamada *et al.*, *Bull. Chem. Soc. Jpn.* **91**, 1196–1204 (2018).
40. R. Brenes *et al.*, *Joule* **1**, 155–167 (2017).
41. Y. Deng *et al.*, *Nat. Energy* **6**, 633–641 (2021).

ACKNOWLEDGMENTS

We acknowledge J. Parker and P. Quinn for support during experiments on the I14 beamline at Diamond Light Source. We thank Diamond Light Source for access and support in use of beamline I14 (proposal number sp20420) and the electron Physical Science Imaging Centre (ePSIC; Instrument E02 and proposal number MG24111) that contributed to the results presented here. Via our membership of the UK's HEC Materials Chemistry Consortium, which is funded by the Engineering and Physical Sciences Research Council (EPSRC; EP/L000202), this work used the ARCHER UK National Supercomputing Service (www.archer.ac.uk). **Funding:** Supported by a National University of Ireland Travelling Studentship (T.A.S.D.); a Newton International

Fellowship funded by the Royal Society and SERB (S.N.); the Royal Society and Tata Group (UF150033) (S.D.S.); EPSRC grant EP/R008779/1 (P.A.M.); the European Research Council under the European Union's Horizon 2020 research and innovation program (HYPERION grant agreement 756962); EPSRC grant EP/R023980/1; a George and Lilian Schiff Studentship, Winton Studentship, EPSRC studentship, Cambridge Trust Scholarship, and Robert Gardiner Scholarship (K.F.); Marie Skłodowska-Curie actions (grant agreements 841136, 841265, and 841386, respectively) under the European Union's Horizon 2020 research and innovation program (D.J.K., E.M.T., and M.A.); scholarships from the British Spanish Society and the Sir Richard Stapley Educational Trust (A.N.I.); an EPSRC studentship (S.M.); the Royal Society (A.A.); a University of Leeds academic fellowship (S.M.C.); an EPSRC studentship (P.C.); EU ERC Advanced Fellowship DLV-835073 (C.P.G.); National Research Foundation of Korea grant 2018R1C1B6008728; and the European Union's Horizon 2020 INFRAIA program (ESTEEM3–grant agreement 823717). **Author contributions:** Conceptualization: T.A.S.D., S.N., S.D.S. Methodology: T.A.S.D., S.N., D.J.K., D.N.J., C.P.G., A.W., P.A.M., S.D.S. Investigation: T.A.S.D., S.N., D.J.K., Y.-K.J., D.N.J., K.F., F.S.R., D.G., A.N.I., E.M.T., Y.-H.C., P.C., M.A., S.M., M.D., S.M.C., A.A. Visualization: T.A.S.D., S.N., D.J.K., S.D.S. Funding acquisition: S.D.S., A.W., C.P.G., P.A.M. Project administration: SDS. Supervision: S.D.S., A.W., C.P.G., P.A.M. Writing–original draft: T.A.S.D., S.N., D.J.K., S.D.S. Writing–review and editing: T.A.S.D., S.N., D.J.K., Y.-K.J., D.N.J., K.F., F.S.R., D.G., A.N.I., E.M.T., Y.-H.C., P.C., M.A., S.M., A.A., M.D., S.M.C., C.P.G., A.W., P.M., S.D.S. **Competing interests:** S.D.S. is a co-founder of Swift Solar Inc. **Data and materials availability:** The data that support the findings of this study are available from the corresponding author upon request and at the Apollo repository (DOI: 10.17863/CAM.78426). All (other) data needed to evaluate the conclusions in the paper are present in the paper or the supplementary materials.

SUPPLEMENTARY MATERIALS

science.org/doi/10.1126/science.abl4890
Materials and Methods
Supplementary Text
Figs. S1 to S19
Table S1
References (*42*–*64*)

27 July 2021; accepted 5 November 2021
10.1126/science.abl4890

Stabilized tilted-octahedra halide perovskites inhibit local formation of performance-limiting phases

Tiarnan A. S. DohertySatyawan NaganeDominik J. KubickiYoung-Kwang JungDuncan N. JohnstoneAffan N. IqbalDengyang GuoKyle FrohnaMohsen DanaieElizabeth M. TennysonStuart MacphersonAnna AbfaltererMiguel AnayaYu-Hsien ChiangPhillip CroutFrancesco Simone RuggeriSean CollinsClare P. GreyAron WalshPaul A. MidgleySamuel D. Stranks

Science, 374 (6575), • DOI: 10.1126/science.abl4890

Stable but not quite cubic

The black, photoactive phase of formamidinium (FA) perovskites, which is usually stabilized by cation alloying to avoid the formation of inactive hexagonal phases, is assumed to be cubic. High-resolution microscopy studies by Doherty *et al*. using nanoscale probes revealed that these FA-rich phases are not cubic but rather undergo slight tilting (by two degrees) of the octahedra. Black phases can have localized regions of hexagonal phases that nucleate degradation. Surface-bound ethylenediaminetetraacetic acid stabilized the tilted phase of pure FA lead triiodide against environmental degradation. —PDS

Science (ISSN) is published by the American Association for the Advancement of Science. 1200 New York Avenue NW, Washington, DC 20005. The title *Science* is a registered trademark of AAAS.